
Since January 2020 Elsevier has created a COVID-19 resource centre with free information in English and Mandarin on the novel coronavirus COVID-19. The COVID-19 resource centre is hosted on Elsevier Connect, the company's public news and information website.

Journal of Molecular Structure 1244 (2021) 130961

Contents lists available at ScienceDirect

Journal of Molecular Structure

journal homepage: www.elsevier.com/locate/molstr

# Synthesis and characterization of new thiazole-based Co(II) and Cu(II) complexes; therapeutic function of thiazole towards COVID-19 in comparing to current antivirals in treatment protocol

Samira A. Almalki[a], Tahani M. Bawazeer[b], Basim Asghar[b], Arwa Alharbi[b], Meshari M. Aljohani[c], Mohamed E. Khalifa[a], Nashwa El-Metwaly[b,d,*]

[a] Department of Chemistry, College of Science, Taif University, P.O. Box 11099, Taif 21944, Saudi Arabia
[b] Department of Chemistry, Faculty of Applied Science, Umm Al-Qura University, Makkah, Saudi Arabia
[c] Department of Chemistry, College of Science, University of Tabuk, Tabuk, Saudi Arabia
[d] Department of Chemistry, Faculty of Science, Mansoura University, Mansoura, Egypt

ARTICLE INFO

*Article history:*
Received 21 May 2021
Revised 12 June 2021
Accepted 21 June 2021
Available online 24 June 2021

*Keywords:*
Thiazol complexes
DFT
In-silico
Pharmacophore
COVID-19 drugs

ABSTRACT

Two thiazole-based complexes were prepared from Co(II) and Cu(II) ions. The new ligand and its complexes were fully characterized by analytical and spectral techniques. The ligand behaved as a neutral tridentate in its keto-form towards the metals *via* O(8), O(10) and O(18) atoms. This was suggested based on the lower shift of $\upsilon$(CH=O), $\upsilon(C=O)_{amide}$ and $\upsilon$(C–O) vibrations. The electronic transitions in Co(II)-HL and Cu(II)-HL complexes displayed *d-d-* transitions which belong to $^4T_{1g}\rightarrow{}^4A_{2g}(F)$ & $^4T_{1g}(F)\rightarrow{}^4T_{1g}$ (P) and $^2Eg\rightarrow{}^2T_2g$, in the two complexes, respectively. ESR spectrum of Cu(II)-HL complex displayed g-factor by the following order; $g_{//}(2.1740)>g_{\perp}(2.0935)>2.0023$, which agrees with octahedral geometry. The geometry optimization was executed by DFT/B3LYP method under valence double zeta polarized basis set (6–31G*), to confirm the structural forms and the mode of bonding. The orientation and the charges of O(8), O(10) and O(18) atoms, support the coordination of the ligand in its keto-form with the metal ions. Pharmacophore profiles were obtained regarding thiazole ligand and other recommended drugs (arbidol, avigan and idoxuridine) that used in treatment protocol of COVID-19 pandemic. Also, query was run in MolPort-library to obtain antiviral analogues, to broaden the search for an effective treatment. Three analogues were obtained for arbidol, avigan and idoxuridine drugs, which have the following numbers; MolPort-047-605-644, MolPort-004-768-508 and MolPort-028-750-709, respectively. Moreover, molecular docking was carried out to obtain all interaction details and rank the efficiency of thiazole compound versus the three antivirals in their interaction with the two COVID-19 proteins. The outcomes suggested the significant antiviral activity of idoxuridine and thiazole (enol-form), which not reach to eliminate the pandemic exactly. While, arbidol and avigan did not have an effective antiviral role, although they still used in COVID-19 treatment protocol.



## 1. Introduction

It is now devastating that the corona pandemic has taken the lives of tens of thousands of people who have put researchers in a race against time to save mankind from this deadly virus, each in its own way or in an open way. The main problem is that this infection cannot be prevented, but the medicines used mitigate the related effects and can succeed with a different virus and fail with Corona. Although promising therapies for the corona family have been found and are currently being studied for COVID-19 in recent decades, the trials have not been completed and all drugs are still being tested [1].

Suspended RNA viruses are coronavirus (severe acute respiratory syndrome) and Middle East respiratory syndrome (Middle East) and retrovirus, which also cause respiratory infection (Ebola and Marburg viruses) [2]. RNA viruses adapt easily to changes because of extremely high rate of viral enzyme errors that are responsible for their genetic replication. Whereas various factors play a part in the creation of diseases, such as genetic variations in the viruses and some environmental factors, these viruses are responsible for many new and re-emerging illnesses [3]. Viruses such as human metapinomavirus and two separate human coronavirus have been present in humans for decades, but species-

* Corresponding author
*E-mail address:* nmmohamed@uqu.edu.sa (N. El-Metwaly).

https://doi.org/10.1016/j.molstruc.2021.130961
0022-2860/

by-species transmission has triggered numerous new viruses from other mammals' or birds' reservoirs such as avian influenza viruses and extreme acute respiratory syndrome (SARS), Corona and Nipah virus. Coronavirus SSR–Cov2 is an RNA virus positive that is infectious to man and is the cause for the current COVID-19 outbreak. It causes RNA virus that is contagious to humans. In December 2019 a new strain of coronavirus was found in Wuhan, China. The virus is also part of SARS and MERS family [4,5].This virus has been documented to be susceptible to high temperatures (heat) and a small number of fat solvents may be inactivated [6].

A broad-spectrum antiviral agent, licensed as an anti-influenza drug, is umifenovir (arbidol). This antiviral agent has been developed for about 25 years for the treatment of influenza A and B in Russia and China at the Institute of Chemical and Pharmaceutical Science in Russia. It has also been patented since 2004 for its therapeutic use against the SARS virus [7]. Favipiravir (avigan), an anti-RNA drug, was developed in Japan for new or recurrent influenza viruses in 2014. To activate and integrate them into viral RNA, ribosyl binding and intracellular phosphorylation is performed by substituting purine nucleosides. RNA-dependent RNA polymerase will then disrupt viruses and prevent elongation of RNA strain and propagate of viruses [8, 9]. Idoxuridine is an antiviral drug for herpes. It is a nucleoside analog, a modified deoxyuridine shape, close enough to be incorporated into the replication of viral DNA, but primary conjugation is prevented by the iodine atom added to the uracil portion. Owing to toxicity, it is only used topically. Initially developed as an anti-cancer medicine, idoxuridine became the first anti-viral agent in 1962 [10, 11].

Owing to their biological properties, heterocyclic compounds are the key structures for the design and synthesis of drugs. One of the most common methods of preparation of heterocyclic compounds [12] is the synthesis of rings by decomposition of suitable linear compounds. Thiazole, due to its numerous medicinal uses, is a strong nucleus. Various biological functions such as antioxidants, analgesics, anti-bacterial, anti-cancer, anti-allergic, antihypertensive, anti-inflammatory, anti-malarial, anti-fungicide and anti-psychotic have been demonstrated by thiazoles [13]. The efficacy of pyrazole-based anti-influenza agent was investigated in a promising study of H1V–viral infection treatment [14]. Moreover, herpes simplex viruses (HSV-1) and HIV-1 reverse transcriptase inhibitors were also seen in pyrazole derivatives [15, 16]. Synthesis of novel thiazole functionalized as a possible HCV inhibitor was advised by docking using structurally dependent approach [17]. The value of tri-substituted thiazoles as anti-flavi-virus targeting compounds [18, 19] was subsequently discussed. Thiazole derivatives have also been identified with antiviral potency against some popular viral diseases. Characterizing a new Schiff base derivatives from 2-aminothiazole which used to prepare VO(IV), Co(II), Ni(II), Cu(II), and Zn(II) complexes for biological uses [20]. The biological activity of three Cu(II) complexes containing benzimidazole derivatives were reported, after their characterization. The antibacterial experiments with E. coli and S. aureus revealed a similar level of response [21].

Based on the above and an attempt by us to participate in finding solutions to this new epidemic, we decided to prepare a new thiazole derivative which used in preparing Co(II) and Cu(II) complexes. Then, characterization process was carried out *via* all possible analyses to assume the molecular and structural formulae of the new compounds. Moreover, molecular modeling was performed to emphasis on these structures suggested. Furthermore, we interested in making a speculative computerized study (in-silico) on new thiazole derivative to find out the extent of activity in inhibiting current corona virus (COVID-19). This in-silico study, was deepened by comparison with three antiviral drugs already recommended in treatment protocol (arbidol, avigan & idoxuridine), which no drug has been able to overcome the virus dangerous until now. This paves the way for the efforts of researchers that is what we did in this research.

## 2. Experimental

### 2.1. Common reagents

The chemicals used to synthesize new thiazole derivative as 2-chloro-N-(thiazol-2-yl)acetamide, salicylaldehyde and $K_2CO_3$ were obtained from Sigma & Aldrich as BDH. While, the salts used to prepare the complexes as $Co(OAc)_2.4H_2O$ and $CuCl_2.2H_2O$, were obtained from Merck. In addition, the solvents used as Ethanol (EtOH), Dimethylformamide (DMF) and Dimethyl Sulfoxide (DMSO) were also obtained from Sigma &Aldrich and have high purity reach to spectroscopic nature therefore used without pretreatments.

### 2.2. Synthesis of 2-(2-formylphenoxy)-N-(thiazol-2-yl)acetamide (HL)

In 20 mL DMSO, salicylaldehyde (0.61g, 5 mmol) was dissolved and applied to a stirred suspension from 2-chloro-N-(thiazol-2-yl)acetamide (0.88 g, 5 mmol)(Scheme 1). The components of the reaction were stirred at 25–30°C for 12 h, poured into ice water and then neutralized by dil. HCl. The solid produced was isolated and recrystallized in EtOH solvent.

Yellow crystals, yield 78%, m.p. = 185–186°C. IR (KBr) (Fig. 1S): 3480 (O–H), 3214 (N–H), 1716 (CH=O), 1681 $cm^{-1}$ (C=O, amide). $^1H$ NMR (DMSO-$d_6$)(Fig. 2S): $\delta$ (ppm) 4.85 (s, 2H, $CH_2$), 7.01 (d, J = 4.00 Hz, 1H, thiazole-H4), 7.13 (t, J = 7.50 Hz, 1H, Ar-H), 7.17 (d, J = 8.50 Hz, 1H, Ar–H), 7.51 (d, J = 4.00 Hz, 1H, thiazole-H5), 7.63-7.67 (m, 1H, Ar–H), 7.74-7.76 (dd, J = 7.50, 2.00 Hz, Ar–H), 10.01 (s, 1H, CHO), 10.44 (s, 1H, NH or OH). Analysis for $C_{12}H_{10}N_2O_3S$ (262.28): Calcd. C, 54.95; H, 3.84; N, 10.68%. Found: C, 54.82; H, 3.87; N, 10.61%. The symbol of ligand used (HL) is referring to labile hydrogen in amide group, which caused keto/enol form of the ligand (Scheme 1).

### 2.3. Synthesis of Co(II) and Cu(II) complexes

The two complexes were prepared by reacting equi-molar ratios (5mmol) from both of metal salt as $Co(OAc)_2.4H_2O$ (1.245 g) or $CuCl_2.2H_2O$ (0.852 g) and thiazole ligand (HL)(1.311 g) in EtOH. The reaction mixtures were kept under reflux for 3hrs. Brown precipitates were filtered off and washed by EtOH. The samples were placed in closed desiccators for dryness under influence of dray $CaCl_2$. Brown $[Co(OAc)(HL)(H_2O)_2].OAc.2H_2O$ complex, Co(II)-HL, yield 67%, m.p.= > 300. Analysis for $C_{16}H_{24}Co\ N_2O_{11}S$ (MW, calcd. 511.37; found, 511): Found (%), C, 37.63; H, 4.71; N, 5.43; Co, 11.20. Calcd (%): C, 37.58; H 4.73; N, 5.48; Co, 11.52. Brown $[Cu(Cl)_2(HL)(H_2O)].3H_2O$ complex, Co(II)-HL, yield 71%, m.p.= > 300. Analysis for $C_{12}H_{18}Cl_2CuN_2O_7S$ (MW, calcd.468.8; found, 414): Found (%), C, 30.96; H, 4.02; N, 5.89; Cl, 15.07; Cu, 13.61. Calcd (%): C, 30.74; H 3.87; N, 5.98; Cl, 15.13; Cu, 13.56. The conductivity

### 2.4. Analysis techniques

From the principle of simplicity, all the devices used for analyzes were shown in the form of pictures in the supplementary file (Scheme 1S), and the specifications of each device were also explained below the image, but the measurement conditions are often written in the discussion part. While the metal and chloride contents were determined by complexometric titration method and gravimetric titration method, respectively [22]

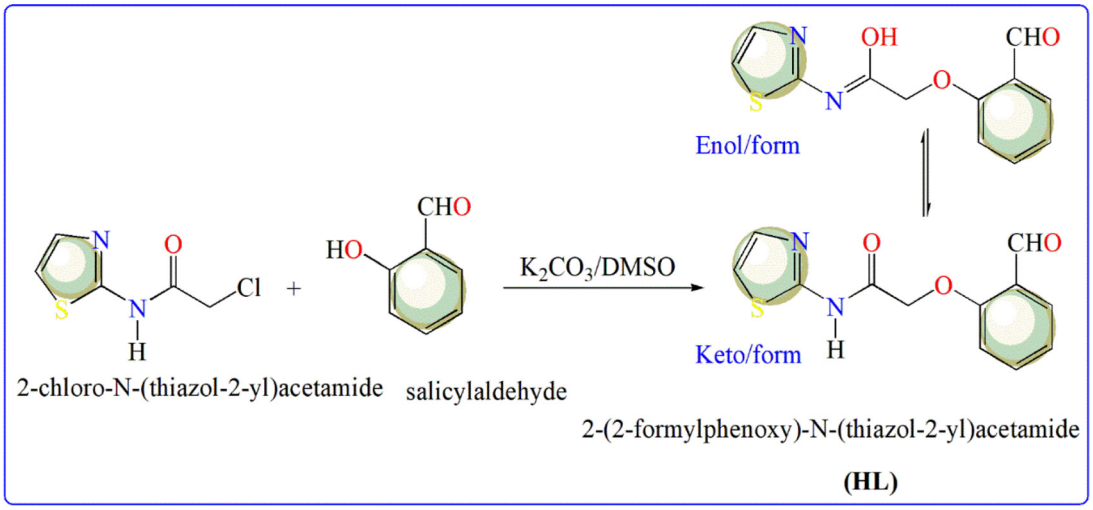


**Scheme 1.** Synthesis steps for thiazole-based ligand (HL).

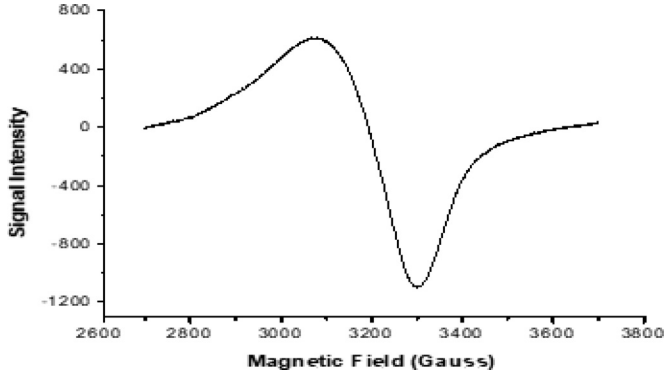


**Fig. 1.** ESR spectrum of Cu(II)-HL complex.

## 2.5. Computational studies

### 2.5.1. Molecular modeling

Gaussian 09 [23] software is a standard molecular modeling program accredited to be used for structural type validation, which approximates to the effectiveness of the single crystal X-ray function. For the DFT operation, Becke3-Lee-Yang-Parr (B3LYP)[23] and valence double zeta polarized basis set (6-31G*) have been added and applied perfectly on the ligand and its complexes. This balanced basis set indicates a split-valence double-zeta plus polarization basis set (6–31G*), which considered the most famous one. This term indicates that the core-orbital is characterized by a contraction of six Gaussian orbitals, while the valence is characterized by two orbitals. The star (*) shows polarization functions on non-hydrogen atoms. Using Integral Equation Formalism Variant (IEF–PCM) and polarizable continuum model, time-based DFT (TD–DFT) [24-26] was conducted at B3LYP level to explore ground and excited state characteristics. To acquire all quantum parameters, the exported computational files (log & chk) were visualized in Gauss-View and Gauss-Sum 2.2 [27] programs. While, the file abbreviated by fchk was obtained from chk file that formulated in Gauss–prog screen.

### 2.5.2. In Silico assay

*2.5.2.1. Pharmacophore query.* Pharmacophore queries were performed (http://pharmit.csb.edu) according to ligand-based search model [28]. The aim of this study is to examine the interaction

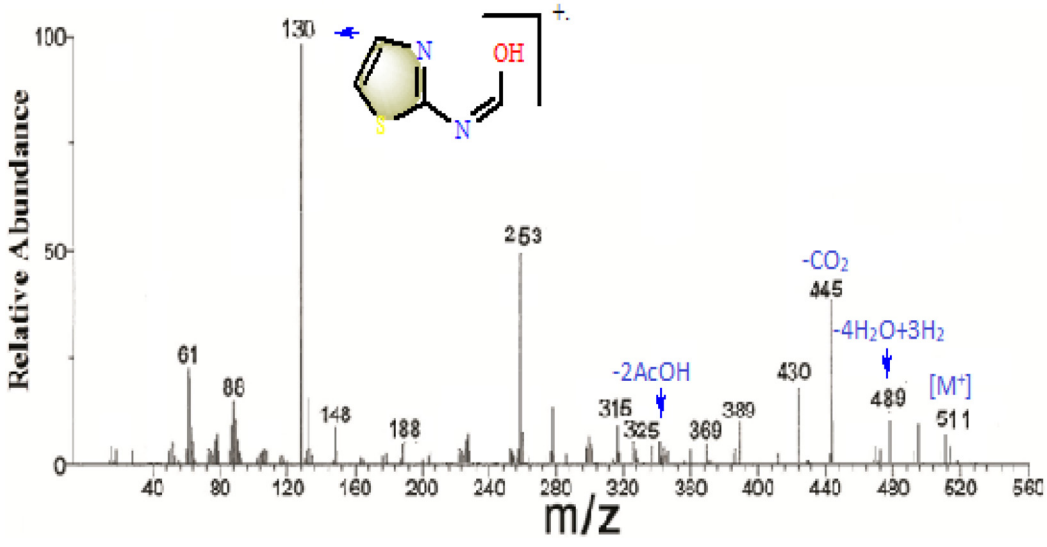


**Fig. 2.** Mass spectrum of Co(II)-HL complex.

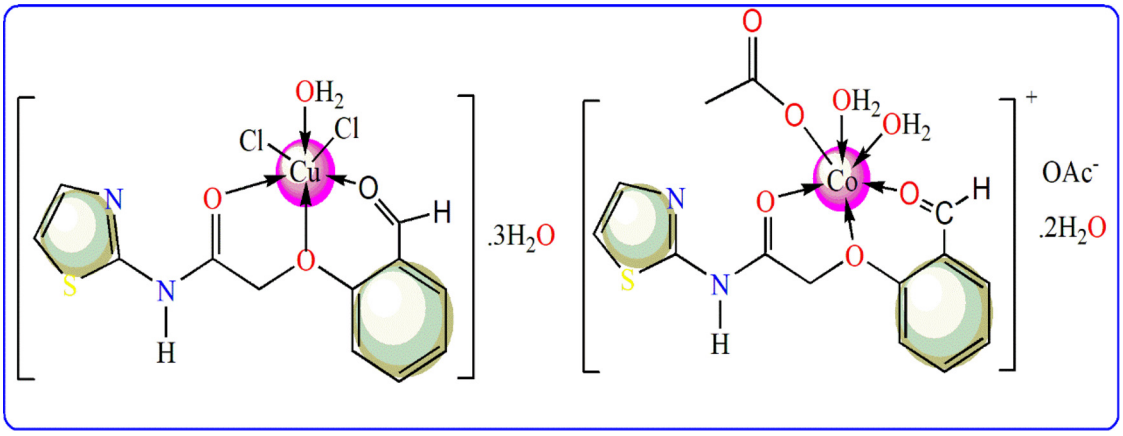


**Scheme 2.** The proposed structures of the complexes.

features of thiazole derivative with two targeted COVID-19 proteins (6lu7 & 7bz5) that assigned from Protein Database (PDB) (Scheme 2S). Furthermore, three recommended drugs such as, arbidol (umifenovir), avigan (favipirovir) and idoxuridine that used for COVID-19 treatment, were also screened to evaluate their antiviral activity in comparing to thiazole-tautomers (keto/enol). In particular, pharmacophore search was performed in MolPort database which containing 7,666,850 molecules correspond to 110,309,969 conformers and this drug-library was updated at 21:12:10, 2020-oct-14. This query aims to reach analogues which may be mimic to the investigated compounds thus expand the search circle for appropriate medicines for this virus and give opportunities to try more medicines, in order to reach the most effective one for this confusing epidemic. The number of H-bonds formed between the drug and COVID-19 proteins could also be determined. H-bond acceptor (H–acc), H–bond donor (H-don), basic (H–bas) and acidic (H–acid) were such bonds reported. Firstly, the format of each compound was adjusted to be suitable for the test and, after fulfillment, a query was done in MolPort database [29]. Three analogues were obtained by a code numbers of, MolPort-047–605–644, MolPort-004–768–508 and MolPort-028–750–709 for arbidol, avigan and idoxuridine, respectively. While, our potential drug (thiazole derivative) did not reveal analogues.

*2.5.2.2. Molecular-docking (MOE).* Molecular Operating Environmental module (ver. 2018) was implemented to collect all interaction features between potential drug (thiazole) or recommended antivirals (arbidol, avigan & idoxuridine) with COVID-19 proteins (6lu7 &7bz5). Such proteins have a proliferation function in COVID-19 cells [30], thus inhibition for these proteins, is a successful target. Accordingly, this in-silico investigation was carried out to evaluate antiviral efficacy of new thiazole derivative as well as the three antivirals. Both of the tested compounds and COVID-19 proteins must be oriented separately before starting each docking process, to be suitable.

Each inhibitor was subjected to energy minimization then measuring the atomic charges and potential energy. These were the phases of sequenced orientation followed by the opening of a new database to save the compound as an MDB format [31]. On the other hand, before adding H-atoms, each protein must get-rid of water molecules from selected receptors and dummies which must adapt according to MMFF-force field. Then, attach receptor types, fix potential energy, and therefore run the site-finder to reach the receptors or dummies that capable for allosteric binding. As a consequence, after choosing the protein-helix, the docking process can be started on the saved MDB-file. The method therefore reaches from 30 poses attempted to the appropriate docking pose. All poses were advanced twice by London dG-scoring function that supported by triangle-matcher [32]. Due to presence of un-preferable clashes between protein pockets and the proposed inhibitors, some poses were declined. The interaction capacity of all compounds tested was measured on the basis of the qualifying hit score and the H-bonding duration, which must be $\leq$ 3.5 Å. The values for the energy score were determined according this relationship; Docking Score (force fields) = - ((interaction energy with receptor /ligand)+ internal energy of ligand) [33]. Furthermore, to determine the inhibition activity against COVID-19 virus cells, the docking patterns as well as the interaction parameters were estimated.

## 3. Results and discussion

### 3.1. General characteristics of complexes

Within the two complexes, the elemental analysis proposed 1:1 molar ratio (M:L). The complexes were insoluble in known organic solvents but fully soluble in DMSO or DMF solvent. In addition, the molar conductivity values ($Ohm^{-1}cm^2mol^{-1}$) for $10^{-3}$mol (in DMSO) reveal the conducting feature of Co(II)-HL complex ($\Lambda_m$= 36.81), while a non-conducting property ($\Lambda_m$= 8.94) for the second one [34]. The high covalence nature of chloride atom was the main cause behind its participation inside the coordination sphere of Cu(II)-HL complex. But, the acetate group has a dual nature regarding its ability for covalent and ionic attachments, which they appeared clearly in Co(II)-HL complex.

### 3.2. Spectral data and mechanism of synthesis

In a very simple approach, it is planned to evolve optimal strategy for the synthesis of 1,3-thiazole-based ligand (HL) and its utilization for the preparation of some metal ion complexes. The synthesis of 2-(2-formylphenoxy)-N-(thiazol-2-yl)acetamide (HL) has been achieved by the reaction of 2-chloro-N-(thiazol-2-yl)acetamide with salicylaldehyde in DMSO in presence of potassium carbonate. The keto/enol form of HL was secured based on compatible spectral analyses. The IR spectrum revealed stretching of O–H group at 3480 $cm^{-1}$, N–H group at 3214 $cm^{-1}$ in addition to two carbonyl groups at 1,716 (aldehyde) and 1681 $cm^{-1}$ (amide)(Fig. 1S). The $^1$H NMR spectrum (Fig. 2S) showed singlet for two protons of methylene group at 4.85 ppm. The doublet signals with coupling constant (J = 4.00 Hz) at 7.01 and 7.51 ppm referred to protons at the fourth and fifth positions at thiazole ring, respectively. The four aromatic protons resonate as triplet (1H), doublet (1H), multiplet (1H) and doublet of doublet (1H) in the re-

**Table 1**
Characteristic IR- bands for thiazole-based ligand and its complexes.

| Comp. | $\upsilon$(OH) | $\upsilon$(NH) | $\upsilon$(C=O) amide | $\upsilon$(CH=O) $\upsilon$(C–O) | $\upsilon$(C=N) | $\delta$(NH) $\delta$(OH) | $\upsilon_{as}$(OAc) $\upsilon_{as}$(OAc) | $\rho_r(H_2O)$ | $\rho_w(H_2O)$ | $\upsilon$(M-O) |
|---|---|---|---|---|---|---|---|---|---|---|
| 1)HL (keto/enol form) | 3480 | 3214 | 1681 | 1716 1112 | 1570 | 1534 1379 | – | – | – | – |
| 2)$[Co(OAc)(HL)(H_2O)_2]OAc.2H_2O$ | B. C. 3526 | 1621 | 1651 1032 | 1588 | 1528 | 1528;1334 | 860 | 615 | 552 | |
| 3)$[Cu(Cl)_2(HL)(H_2O)].\ 3H_2O$ | 3518 | 3186 | 1632 | 1650 1099 | 1595 | 1543 | – | 887 | 607 | 506 |

B.C., broad centered; the repetition of assignment value due to overlapping between near vibrations.

**Table 2**
Magnetic moments, electronic transitions and ligand field parameters.

| Compound | $\mu_{eff.}$ (B.M.) | Intraligand and CT transitions | d-d transitions; Assignments ($cm^1$) | 10Dq($cm^{-1}$); $\beta$, B ($cm^{-1}$); $\upsilon_1$($cm^{-1}$) | Geometry | |
|---|---|---|---|---|---|---|
| Co(II)-HL | 4.73 | 40,816; 32,787 25,381 | 15,385;($\upsilon_2$) 19,231 ($\upsilon_3$) | $^4T_{1g}$ (F)→ $^4A_{2g}$(F) $^4T_{1g}$ (F)→ $^4T_{1g}$(P) | 8285.46; 0.898; 872.15; 7216.0 | Octahedral |
| Cu(II)-HL | 1.70 | 32,258; 28,169 25,773 | 22,472; 17,544 | $^2Eg \rightarrow {}^2T_2g$ | –– | Octahedral |

CT; Charge Transfer

gion from 7.13 to 7.76 ppm. The singlet signals at 10.01 and 10.44 ppm attribute to protons of formyl (CH=O) and N–H (in keto form) or OH (in enol form) groups, respectively.

Comparing the vibrational bands appeared in Co(II)-HL or Cu(II)-HL spectrum (Fig. 1S) with that in the corresponding ligand, reveals significant changes which were summarized (Table 1) to known the mode of bonding inside the coordination sphere [35]. The broadness remarked in complexes spectra may refer to existence of high number of water molecules, but we could estimate significant changes upon $\upsilon$(CH=O), $\upsilon(C=O)_{amide}$ and $\upsilon$(C–O) vibrations. These bands were shifted from 1716, 1681 and 1112 $cm^{-1}$ values that appeared respectively in free ligand spectrum [36]. The shift to higher wavenumber observed for $\upsilon$(C=N) vibration, reveals its ruling out from coordination. The presence of anionic acetate group in Co(II)-HL spectrum, was suggested firstly based on molar conductivity value (36.81 $ohm^{-1}cm^2\ mol^{-1}$) as well as the appearance of $\upsilon(OAc^-)$ at 1435 $cm^{-1}$. Whereas, the mono-dentate acetate group was appeared at 1,528 and 1,334 $cm^{-1}$ that assign for $\upsilon_{as}$(OAc) and $\upsilon_s$(OAc), respectively. In addition to remarkable broadness in IR-spectra of the complexes, $\rho_r(H_2O)$ and $\rho_w(H_2O)$ vibrations were appeared and assigned to confirm presence of water molecules. Finally, $\upsilon$(M–O) band was appeared at lower wavenumber region (552 & 506 $cm^{-1}$) in the two complexes, respectively [37].

### 3.3. UV-Vis spectra and magnetic moments

The effect of UV-Vis radiation on the dissolved amount from Co(II)-HL or Cu(II)-HL complex (in DMF) was drawn from 200 to 900 nm range (Fig. 3S). The excitation of electrons from n, $\sigma$ and $\pi$ orbitals was appeared in the following transitions; $\pi \rightarrow \pi^*$ (C=O, C=N), n→ $\sigma^*$ (OH or NH) and n → $\pi^*$, sequentially in deep UV region (Table 2). The presence of metal ions was correlated with the presence of ligand field transitions (d-d), which occurred legally due to ligand coordination [38]. The d-d transitions in Cu(II)-HL complex spectrum, were appeared at 22,472 and 17,544 $cm^{-1}$ which attribute to $^2Eg \rightarrow {}^2T_2g$ transition in distorted octahedral geometry (Scheme 2). The magnetic moment value of the complex close to spin only moment (1.73 B.M.).

On the other side, d-d transitions recorded in Co(II)-HL complex spectrum, were at 15,385($\upsilon_2$) & 19,231($\upsilon_3$), which attributed to $^4T_{1g}(F)\rightarrow {}^4A_{2g}(F)$ and $^4T_{1g}(F)\rightarrow {}^4T_{1g}(P)$ transitions, respectively [39]. The magnetic moment value of Co(II)-HL complex (4.73 B. M.) coincides with octahedral geometry (Scheme 2)[39]. Moreover, the parameters of ligand field in this complex, as a crystal field stabilization energy (10Dq, $cm^{-1}$), nephelauxetic ratio ($\beta$) and Racah parameters (B, $cm^{-1}$) beside the first transition band ($\upsilon_1$) were calculated (Table 2) by known relations [37]. The values were appeared normal with distorted octahedral that has high degree of ionic characteristic for new Co-L bonds [40].

### 3.4. Thermogravimetric analysis

For the two complexes, TGA curves were obtained to differentiate between the types of water molecules coordinated or hydrated according to the degree of thermal stability reported. The curves were obtained (Fig. 4S) from thermogravimetric analyzer at constant heating rate (10 °C $min^{-1}$) over a temperature range of 20-1000°C and in inert atmosphere (liquid nitrogen). The TGA curves reflect the lower thermal stability of the complexes that have begun their thermal decomposition at lower temperatures (89.8 or 51.3 °C).

This step was followed by other two successive steps till ~ 610 °C. The second step started at ~ 150 °C, corresponds to expel of coordinating water molecules beside other molecules as $CH_3COOH$, CO or $Cl_2$. The third step which began at ~430 °C, corresponds to a part from the ligand decomposed (Table 1S). Whereas, the high percentage (~50 %) of the residual part for each complex emerged, suggesting the stability of coordination-sphere that centered by the metal ion. The relative consistency between the mass losses (%) calculated and found, points to the precise identification of the step boarders and no chance for overlapping between successive steps.

### 3.5. ESR spectrum of Cu(II)-HL complex

Electron paramagnetic resonance is an important tool for further verification of structural forms previously proposed in UV-Vis part. The complex of $d^9$ system was scanned at $\upsilon$ = 9,435 GHz (DPPH standard, 25°C) (Fig. 1). For resolved microstates (ml = 3/2, 1/2, -3/2 &-1/2), four hyperfine splitting lines (S = 1/2, I = 3/2) in the complex were expected, while the lack of resolution caused difficulties in calculations. Hamiltonian g-factor values were calculated and ranked by $g_{//}$ (2.1740) > $g_{\perp}$ (2.0935) > 2.0023, which coincides with octahedral geometry that has ground term of $^2A_1g$ ($d_X{}^2\text{-}_Y{}^2$) [41]. The g-values are highly influenced by spin-orbital coupling ($\lambda$ = -828) which were modified significantly after complexation. The parameter G for exchange interaction was deter-

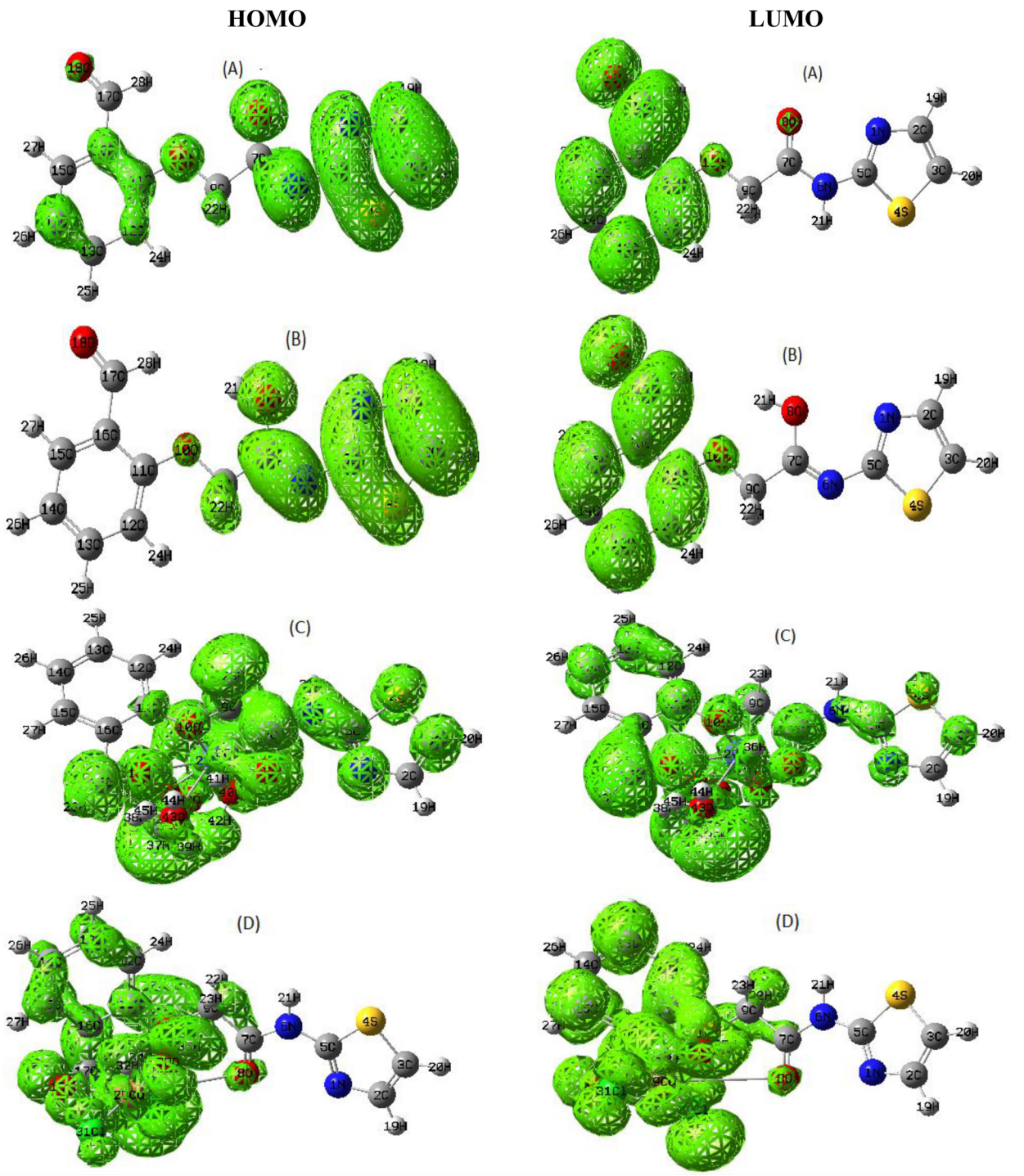


**Fig. 3.** Frontier orbitals of the keto(A)-enol (B) form of the ligand and its Co(II)-HL (C) and Cu(II)-HL (D) complexes.

mined (1.883) and the value was slightly lower than the usual (G = 4). This lowering may refer to metal-metal interaction between adjacent molecules that effects on the clarity of hyperfine splitting. The tetrahedral distortion index ($f = g_{//}/A_{//}$) has also been determined and the value (129.143) is relatively similar to the octahedral configuration value [42].

Furthermore, isotropic and anisotropic indexes ($A_o$ & $g_o$) were estimated by using these relations; $A_o$ (102.39) $= (A_{//} + 2A_{\perp}) / 3$ and $g_o$ (2.1203) $= (g_{//} + 2g_{\perp}) / 3$. Due to complexation as well as geometry distortion, the measured values deviated considerably from free electron. The Fermi-contact term that measured the effect of unpaired electron on the inner atomic-core, was also measured (k). This index was calculated from this relation; $K = -(A_o / p)-(g_e - g_o)$ and the value (0.0072) is normal. The in-plane $\sigma$-bonding ($\alpha^2$) and $\pi$-bonding ($\beta^2$) values, were estimated from these successive relations; $\alpha^2$ (0.7184) $= (A_{//} / 0.036)+(g_{//} - 2.0023)+3/7(g_{\perp} - 2.0023)+0.04$ and $\beta^2$ (0.6330) $= (g_{//} -2.0023) E/(-8\lambda\ \alpha^2)$, where E ($\upsilon_1$) = 17,544 $cm^{-1}$. These values indicate the covalent characteristic of new Cu-L bonds (near 0.5). Furthermore, the dipole term was estimated by using this relation $P(255.52) = 2\ \gamma Cu\ \beta_o\ \beta_N/(r-3)$, where, $\gamma Cu$ is the magnetic moment, $\beta_N$ is the nuclear magneton, $\beta_o$ is the Bohr magneton and r is the ionic ra-

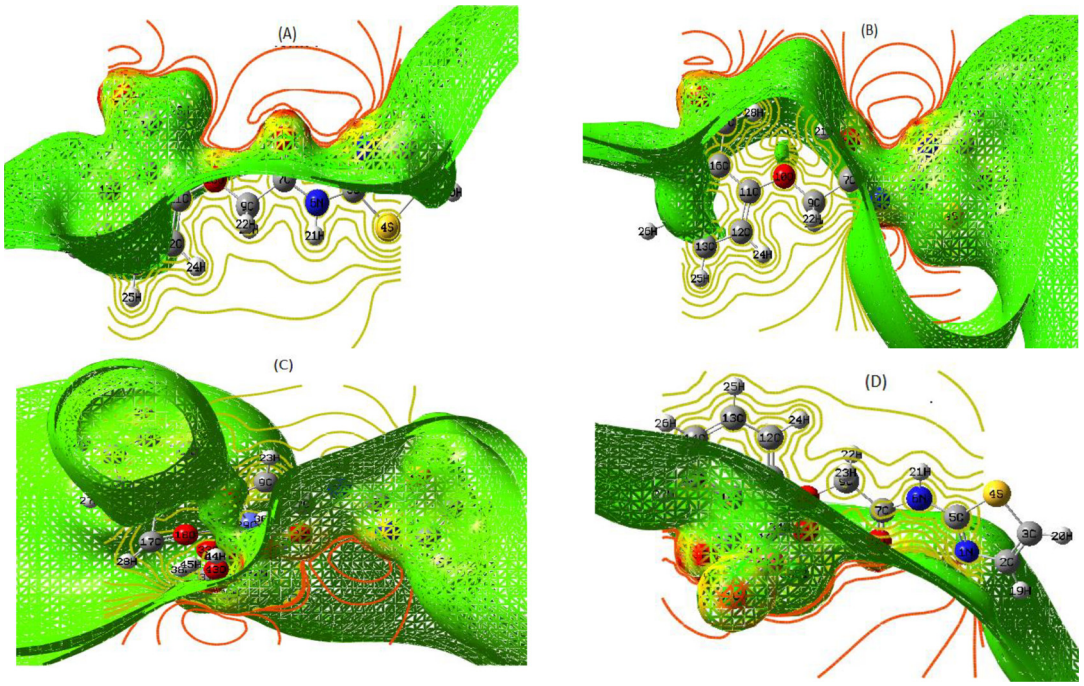


**Fig. 4.** Iso-surface with array plots of the keto(A)–enol (B) form of the ligand and its Co(II)-HL (C) and Cu(II)-HL (D) complexes.

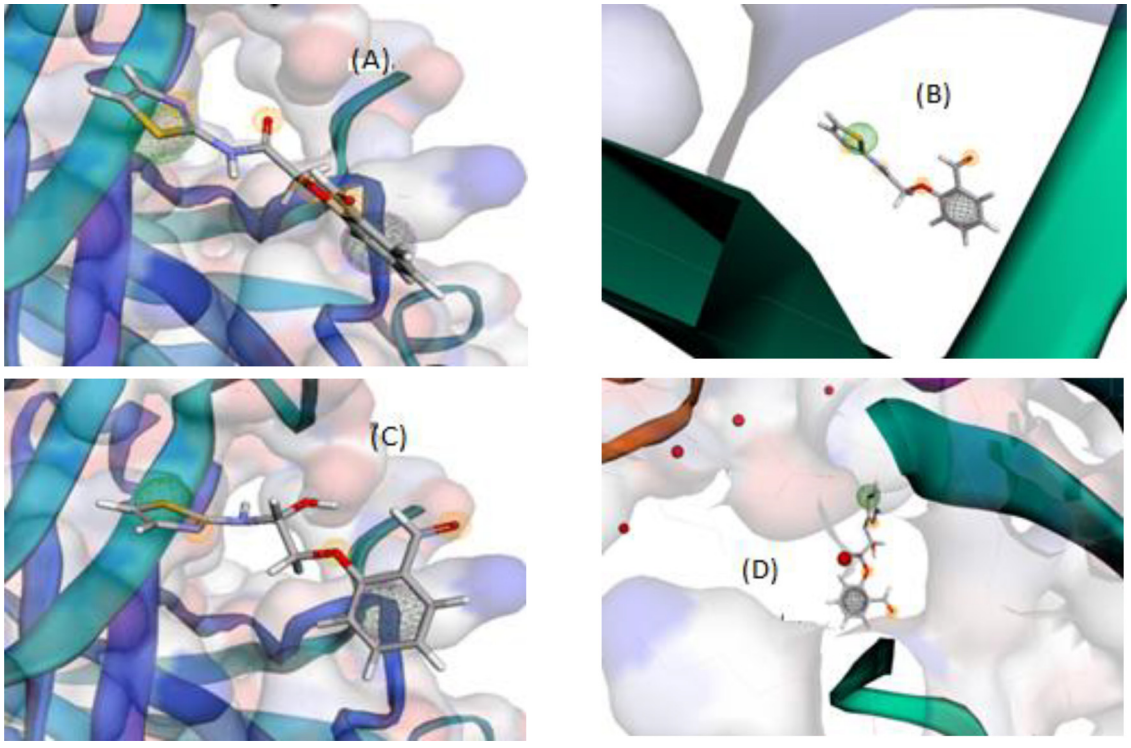


**Fig. 5.** Pharmacophore query for keto (A, B)–enol (C, D) forms of the ligand towards 7bz5 and 6lu7, respectively, as COVID-19 proteins.

dius [43]. Finally, these parameters seemed natural with that indicated by octahedral geometry which have substantial covalent characteristic for Cu(II)-L bonds.

### 3.6. Mass spectral analysis

This analytical platform provides further evidence for the molecular formula that suggested for the complexes (Fig. 2 & 5S), particularly in the lack of ability to isolate single crystal suitable for crystallographic analysis. This scanning was done at heating rate of m/z = 50–1000 and below 40°C/min at 70 eV. The collision-induced ionization was achieved by a beam of electrons after evaporating the compound, which leads to molecular ion that successfully fragmented to other small masses. These fragments were sorted according to their mass/charge values which recorded in the patterns displayed (Fig. 2 & 5S).

The fragmentation pattern of Co(II)-HL complex exhibited the molecular ion peak at m/z = 511 (I=12), which matches per-

fectly [$M^+$] ion. This ion that subjected to accelerated electrons reveals a consecutive fragmentation peaks (Fig. 2), among that, the base peak (I=100%) which assigned (typed in the figure). Furthermore, the spectrum of Cu(II)-HL complex was also obtained (Fig. 5S) and the molecular ion peak was recorded at m/z = 414 (I = 9, calcd. 468.8), which is completely different from the calculated one. This could being explained due to expel of crystal water molecules during initial vaporization step before electrons-bombardment. This behavior is usually happened as reported in many publications [44], consequently the molecular ion may attribute to [$M^+$–3($H_2O$)]. Finally, it is pleasant to note that, the peaks appeared at m/z = 61 in Co(II)-HL, or appeared at m/z = 65 in Cu(II)-HL spectrum, denote to metals isotopes that basically exhibited during fragmentation of complexes.

### 3.7. XRD of Cu(II)-HL complex

The dynamics of crystal-lattice, purity and the degree of consistency within the crystal framework are discussed in this method of analysis. A powdered sample from Cu(II)-HL complex was targeted by X-ray beam that induced from Cu/K$\alpha$1 radiation-source in the range of $10^\circ < 2\theta < 80^\circ$. The diffracted x-rays draw the peaks shown (Fig. 5S). This pattern represents a well nano- crystallinity of the particles and the crystal parameters were being estimated easily according to FWHM method [45]. FWHM, crystallite-sizes(Å), $2\theta$, d spacing (Å), relative intensity, crystal strain ($\varepsilon$) and dislocation density ($\delta$), were easily calculated for such crystalline system by using equations that are so simple [46]. Sequentially, the calculated values were 0.2821, 5.334, 31.5510, 2.83335, 2810, 3.766 and 0.0351. The particle size was appeared in nanometer range, also the crystal strain or dislocation points to the well construction of crystal [46].

### 3.8. Computational study

#### 3.8.1. Geometry optimization

The use of advanced molecular modeling program as Gaussian 09 [23] aims to confirm the structural shapes of the new compounds and then extract many data that are not less important than those extracted from x-ray single crystal, in confirming the chemical bond. We tried to isolate single-crystal for the complexes but we completely failed, so from using Gaussian 09 program, we can get the closest visualization for chemical structures and compare them with that assumed from spectroscopic studies.

*3.8.1.3. Global reactivity features.* By using DFT/B3LYP method, we optimized the geometry of the ligand tautomer-forms (keto/enol) and its new complexes. Under valence double zeta polarized basis set (6–31G*), the TD–DFT methodology was employed. In order to obtain the best geometry (Fig. 7S), as well as 3D-maps of frontier orbitals (Fig. 3), electrostatic potential (MEP) (Fig. 8S) and iso-surface with array plots (Fig. 4), all exported files were visualized.

The optimized geometry of HL ligand displayed distinctive arrangement for HC(17)=O(18), C(9)-O(10) and C(7)=O(8) groups, that indicates their high opportunity for coordination with metal ions, as already suggested. Furthermore, the charges on donor sites of HL keto-form were; O(18)(-0.389824), O(10) (-0.539062), O(8)(-0.344114), S(4) (0.470460), N(6) (-0.314299) and N(1)(-0.283715) [47]. These values exhibited the high negative charges of coordinating atoms as O(18), O(10) and O(8). This appearance reflects their high affinity towards coordination with the metal ions than the other sites, which suffer minimization in their negative charges and moreover one positively charged atom (S). While, such charges in the enol-form were; O(18)(-0.380713), O(10)(-0.536449), O(8)(-0.121452), S(4) (0.527769), N(6) (-0.402702) and N(1)(-0.282545). As seen, the negative charges on most atoms were minimized, which explains the preferable coordination of keto-form of ligand than the enol-form.

Furthermore, the formation energy (E, a.u.), dipole moment (D, Debye), $E_{HOMO}$ (eV), $E_{LUMO}$ (eV) and $\Delta E$ ($E_{LUMO}$ -$E_{HOMO}$, eV) were estimated for both tautomer forms to be, -1196.33; 9.0126; -0.2401, -0.0616 and -0.1784 in the keto-form, while were, -1196.31; 4.3234; -0.2299; -0.0746 and -0.1553 in the enol-form. The values of formation energy and the energy gap between frontier orbitals ($\Delta E$) reflect the stability of the keto-form. Also, the high dipole moment of the keto-form facilitates its coordination. Finally, these data pushed to the priority of keto-form in coordination, which already suggested from the spectral analyses. Moreover, these parameters were also extracted for the two complexes and their values in Co(II)-HL complex were, -2934.06; 11.9815; -0.1112; -0.0634 and -0.0478, while in Cu(II)-HL complex were, -3831.79; 15.898; -0.15837; -0.09367 and -0.0647, respectively. The high dipole moment values of the complexes, clarify their high polarity, which leads to lower their lipophilicity and decrease the miscibility in living-cell lipids. Consequently, the biological efficiency of theses complexes may be very low, so we excluded them from our in-silico assay.

*3.8.1.4. Characteristics of maps demonstrated on cubic contours.* 3D-maps of HOMO & LUMO levels were demonstrated over new contours to explain the distribution of electrons on the functional groups (Fig. 3). With respect to the ligand tautomer-forms, the two orbitals appeared covering the coordinating centers as O(8), O(10) & O(18) in the keto-form while the enol-form excluded O(8) & O(18) atoms. This indicates the extent of fluency in electronic transitions inside the coordinating functional groups in the keto-form than that in the enol-form, which supports the priority for keto-form coordination [48]. On the other hand, the two orbitals appeared more focused on the area of central atoms inside the two complexes.

Furthermore, other two maps were built on surface contours to extract essential features, such maps were the molecular electrostatic potential (MEP) (Fig. 8S) and iso-surface with array plot (Fig. 4). MEP-map discriminates nucleophilic, electrophilic and neutral zones in the ligand tautomer forms to measure the nucleophilicity of groups towards the metal ions thus confirming the binding mode. These three zones were appeared in the maps by red, blue and green colors, respectively. The electrostatic potential range in the keto-form was from -5.677e-2 to 6.677e-2, while that in the enol form was from -4.706e-2 to 5.706e-2. The range in the keto-form appeared broad than that in the enol-form, which clarifies the intensive polarity in the keto-tautomer. Also, the red zone was notably focused on coordinating centers [O(8), O(10) &O(18)] of the keto form, while N(6) atom appeared has electrophilic property that supports its exclusion from coordination.

On the other side, it is interesting to demonstrate iso-surface with array plot (Fig. 4) for the tested compounds to determine the degree of unsaturation for outer couture and confirm the electrostatic features of MEP-maps. Such iso-surface map could being created by measuring electron density at many points over the surface grid, then connected to obtain the final shape (Fig. 4). Also, the array plots (2D) were created to separate inner contour by its yellow lines from the outer contour by its red lines. As seen, the value of iso-surface outer contour is lower than that of inner contour. This indicates the ability of surface to acquire electrons from surrounding or from inner contour during excitation, due to unsaturation level of the outer surface [48].

#### 3.8.2. In-silico assays towards COVID-19

This computation aims to simulate the behavior of our new thiazole derivative (keto/enol forms) towards current corona virus (COVID-19) based on therapeutic history of thiazole compounds.

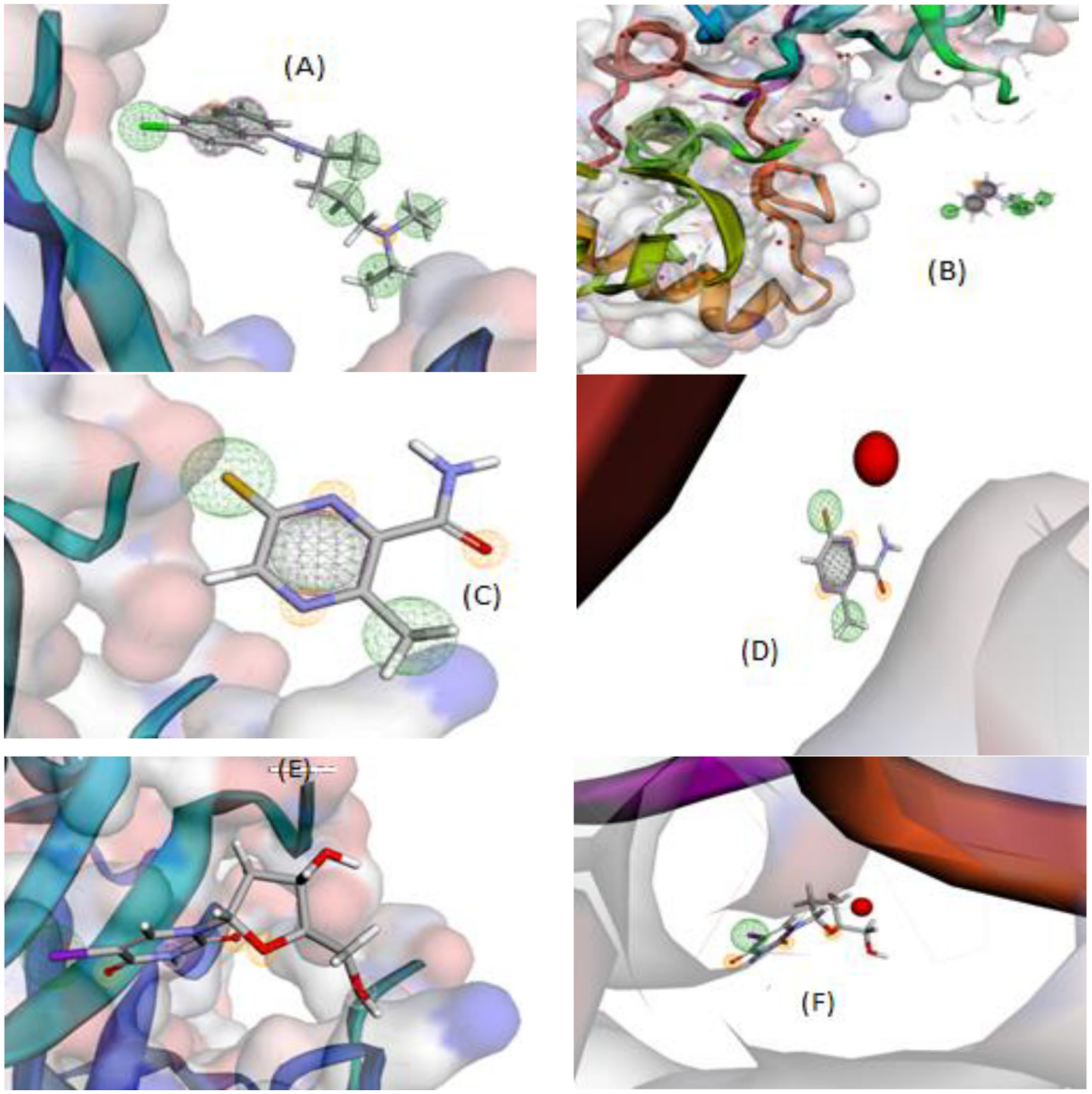


**Fig. 6.** Pharmacophore query search for arbidol(A, B), avigan (C, D) and idoxuridine (E, F) towards 7bz5 and 6lu7, respectively, as COVID-19 proteins.

This study was deepened by comparison with three known drugs as arbidol, avigan & idoxuridine that are now used in treatment protocol but could not solve the problem. This paves the way for efforts to search on other effective drug that we tried in this research. The selected proteins for this study as the entry of COVID-19, were 7bz5 and 6lu7, which were characterized according to Protein Database (PDB) and displayed (Scheme 2S)

*3.8.2.5. Pharmacophore profile.* To build interactive environment that conducts to simulate interaction between three selected drugs (arbidol, avigan & idoxuridine) and our potential one (thiazole) with COVID-19 proteins (7bz5 & 6lu7), we used Pharmit link. Furthermore, pharmacophore profiles were obtained through searching in MolPort-library till reach to analogues that play the same therapeutic role, to broaden the search for an effective treatment for such pandemic virus. This process was run based on ligand-type through grid-type, to get a brief view about the interaction features among that the number and kind of H-bonding formed between sites and receptors [49]. As seen in the patterns (Figs. 5 & 6), the behavior of thiazole ligand is clearly close to the behavior of the tested antivirals. The interaction of all compounds with 7bz5 protein was appeared significant than that with 6lu7 one, except thiazole-enol form, which displayed notable interaction with 6lu7. The H-bonding formed were H-donor (H-don) and H-acceptor (H-acc) only which also counted (Table 4). Also it is worthy to note that, the queries conducted in MolPort- library discovered three analogues for arbidol, avigan and idoxuridine drugs. (Scheme 3). These analogues are numbered by MolPort-047–605–644, MolPort-004–768–508 and MolPort-028–750–709, respectively. Whereas, there is no analogues for new thiazole ligand in its forms (keto/enol), which is normal for new designed-drug.

These results explained the high correlation coefficient values (0.7107, 0.920 & 0.784) and lower Room-Mean-Square deviation (RMSD) values that were 0.351, 0.084 & 0.289, respectively with the three analogues [50]. These values point to the best interaction behavior of avigan-analogues that has a number; MolPort-004-768-508, which may be used in treatment for COVID-19 virus, also.

*3.8.2.6. Simulation for docking behavior towards corona-virus.* A) Inhibition activity towards COVID-19

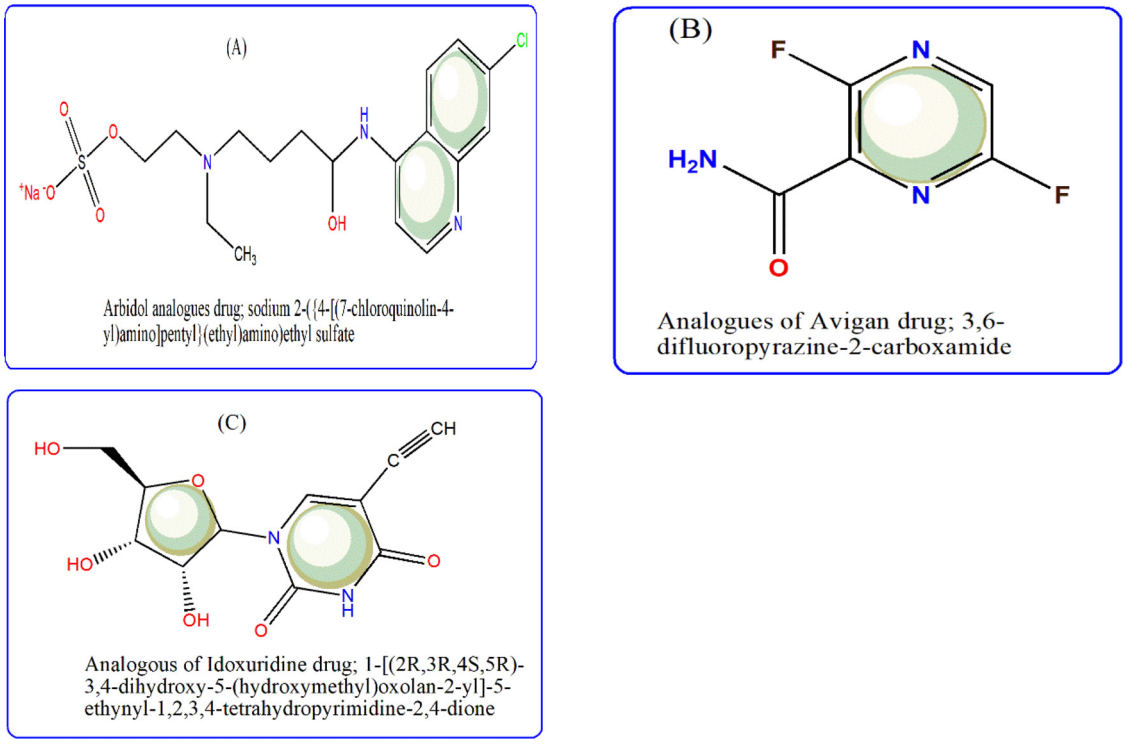


**Scheme 3.** Pharmacophore analogues drugs obtained from MolPort library for arbidol, avigan & idoxuridine (A,B,C).

**Table 3**
Interaction parameters for docking poses for HL ligand and current drugs towards COVID-19 proteins.

| Compounds | Proteins | ligand | Receptor | Interaction | Distance(Å) | E(Kcal/mol) | S(energy score) | Acceptor bonds | Donor bonds |
|---|---|---|---|---|---|---|---|---|---|
| HL(Keto/form) | 6lu7 | –- | –- | –- | –- | –- | -5.828 | 4 | 1 |
| | 7bz5 | 5-ring<br>5-ring | CA TYR 473 (A)<br>N GLN 474 (A) | Pi-H pi-H | 4.25 3.69 | -0.9 -2.2 | -5.0205 | 4 | 1 |
| HL(Enol/form) | 6lu7 | N6 5-ring | O HIS 164 (A)<br>5-ring HIS 41 (A) | H-donor<br>pi-pi | 3.09 3.78 | -2.1 -0.0 | -5.9171 | 4 | 2 |
| | 7bz5 | –- | –- | –- | –- | –- | -5.1185 | 4 | 2 |
| Arbidol(Umifenovir) drug | 6lu7 | C17 | 5-ring HIS 41 (A) | H-pi | 3.68 | -0.6 | -7.0452 | 2 | 1 |
| | 7bz5 | 6-ring | 5-ring TRP 436 (A) | Pi-pi | 3.96 | -0.0 | 5.6959 | 2 | 1 |
| Avigan (Favipiravir) drug | 6lu7 | C8 | 5-ring HIS 41 (A) | H-pi | 4.21 | -1.8 | -4.4133 | 3 | 1 |
| | 7bz5 | – | –- | –- | –- | –- | -4.2014 | 3 | 1 |
| Idoxuridine drug | 6lu7 | C3 N6 O14 O16 | O HIS 164 (A)<br>SD MET 49 (A)<br>SG CYS 145 (A)<br>NE2 HIS 163 (A) | H-donor<br>H-donor<br>H-donor<br>H-acceptor | 3.17 3.10<br>3.27 2.93 | -0.9 -4.5<br>-1.9 -2.2 | -6.1962 | 5 | 3 |
| | 7bz5 | C3 O14<br>6-ring | OD1 ASN 343 (A) O PHE 342 (A) | H-donor<br>H-donor<br>Pi-pi | 3.37 3.01<br>3.80 | -1.2 -1.9<br>-0.0 | -5.1074 | 5 | 3 |

Although we have tested the interaction validity of the antivirals (arbidol, avigan & idoxuridine) and our designed one (thiazole) using Pharmit link, however, the interaction information is incomplete and insufficient to judge the efficiency of these compounds. So we implemented MOE-docking module to put the closest view to what happen inside COVID-19 cells when treated with the three antiviral drugs and our potential one (thiazole). This docking strategy was already certified from drug-designing industry to evaluate the biological activity of either designed compound before its synthesis, or to simulate the interaction path of known drug and extract all interaction features with protein pockets. Both of the two aims were applied here, our potential antiviral before practical use as well as the three recommended antivirals that already used. To determine the inhibition efficiency of each tested compound intentionally, the docking processes were performed and the most effective interaction poses (Figs. 9S–12S) as well as the docking parameters (Tables 3 & 4) were achieved. consequently we aggregated the following remarks from docking outcomes, to rank the antiviral activity for all tested compounds and throw a light on the best in between; i) The scoring energy values suggest the antiviral activity order towards 6lu7 protein as follow; arbidol (-7.045) > idoxuridine (-6.1962) > enol-form (-5.9171), while towards 7bz5 protein as follow; arbidol (-5.6959) > enol-form (-5.1185) > idoxuridine (-5.1074) [51]. Unfortunately, the docking poses of arbidol and avigan

**Table 4**
Binding affinity parameters for the docking complexes with COVID-19 proteins.

| The docking complex | Total energy (Kcal/mol) | Electronic energy (Kcal/mol) | Heat of formation (Kcal) | Ionization potential (eV) | Sum of atomic polariazability |
|---|---|---|---|---|---|
| 1)Keto HL-6lu7 | -74756.054 | -422191.62 | -27.1462 | 9.0727 | 35.2939 |
| 2)Keto HL-7bz5 | -74755.414 | -425670.43 | -26.4334 | 9.3037 | 35.2939 |
| 3)Enol HL-6lu7 | -75403.851 | -438473.65 | -45.1254 | 9.1801 | 36.6275 |
| 4)Enol HL-7bz5 | -75399.757 | -443045.96 | -41.0319 | 9.0144 | 36.6275 |
| 5)Arbidol-6lu7 | -84338.835 | -634783.93 | 28.3387 | 8.7870 | 54.4966 |
| 6)Arbidol-7bz5 | -84337.656 | -613853.68 | 29.5221 | 8.5604 | 54.4966 |
| 7)Avigan-6lu7 | -52500.816 | -224627.42 | -37.7525 | 10.0705 | 19.2198 |
| 8)Avigan-7bz5 | -52500.839 | -224632.92 | -37.7707 | 10.0730 | 19.219 |
| 9)Idoxuridine-6lu7 | -84576.679 | -472147.09 | -169.222 | 9.7855 | 34.7347 |
| 10)Idoxuridine-6bz5 | -84576.796 | -472302.46 | -169.3357 | 9.8431 | 34.7341 |

drugs have a bond lengths over 3.5 Å, which considered as untrue docking paths that must be ignored. While, the docking paths of idoxuridine and thiazole (enol-form), were considered true ($\leq$ 3.5 Å), which we will interest in these details. This denotes the superiority of antiviral idoxuridine drug, while our potential drug (thiazole) exceeds in its efficiency antiviral avigan drug. ii) The effective interacting sites were 5–ring, C3, N7, O14 and O16 *via* H-don and H-acce mainly, towards the following amino acid residues; HIS164, 163, 41; MET49; CYS145; ASN343 and PHE342 [52]. iii) The polar receptors that appeared as a pink circles were the mainly interacting receptors in the docking poses except idoxuridine-7bz5 complex that exhibited the interaction of neutral receptors (green circles) (Figs. 9S-12S). iv) Ligand exposure surface was appeared lower, while the receptor surface (surface around the circles) and proximity contour (dotted-lines surround the compound) appeared broad. This indicates the extent of saturation for interacting sites which may not accept extra-bonding from receptors. Also, the efficiency of these compounds appeared in its maximum state and cannot being elevated. vi) The lower energy content which reaches up to -2.1 and -4.5 Kcal/mol, reflects the mild stability of obtained docking complexes [52]. Finally, the antiviral activity of idoxuridine and thiazole (enol-form) is significant but not reach to eliminate the pandemic exactly. While, arbidol and avigan did not have an effective antiviral role, although they still used in COVID-19 treatment protocol.

A) Binding affinity property

We measured certain docking parameters to demonstrate the binding affinity of the tested compounds (drugs and thiazole-tautomers) (Table 4). The targeted parameters were the total energy, electrostatic energy, formation heat, ionization potential and amount of atomic polariazability, to validate earlier statements. Lower energy content of docking complexes that belong to idoxuridine, arbidol & thiazole, indicates their stabilized complexes. While, excluding arbidol from comparison puts idoxuridine and thiazole to be in the foreground. Exothermic property of the heat of formation that appeared with idoxuridine and thiazole after excluding avigan, asserts on their stability. Also, the lower ionization potential and atomic polariazability of them, indicate the facilitated interaction with COVID-19 proteins [53].

## 4. Conclusion

Thiazole-based ligand was used to synthesize Co(II) and Cu(II) complexes, after isolating the solid products, they were characterized by variable analytical and spectral techniques. The ligand was coordinated in its keto-form *via* tridentate mode of bonding within the octahedral geometry that centered by metal ions. This mode was firstly supported by spectral analysis and finally by the computational data that extracted from Gaussian 09 program by applying DFT/B3LYP method under valence double zeta polarized basis set (6–31G*). In-silico assays were applied on thiazole derivative as a potential antiviral in comparing to three antivirals (arbidol, avigan and idoxuridine) that already used in COVID-19 treatment protocol. This computational assessment was performed through pharmacophore query in MolPort-library and by using MOE-docking module. All interaction features were obtained and the antiviral activity was ranked to clarify the priority of idoxuridine and thiazole derivative. While, arbidol and avigan did not have an effective antiviral role, despite of their use in COVID-19 treatment protocol till now.

## Declaration of Competing Interest

The authors declare that they have no known competing financial interests or personal relationships that could have appeared to influence the work reported in this paper.

## Acknowledgment

Dr. Mohamed acknowledge Taif University Researchers Supporting Project number (TURSP-2020/43). Taif University, Taif, Saudi Arabia

## Supplementary materials

Supplementary material associated with this article can be found, in the online version, at doi:10.1016/j.molstruc.2021.130961.

## References

[1] M. Refat, A. Sedayo, A. Sayqal, A. Alharbi, H. Katouah, H. Abumelha, S. Alzahrani, F. Alkhatib, I. Althagafi, N. El-Metwaly, Aurintricarboxylic acid and its metal ion complexes in comparative virtual screening versus Lopinavir and Hydroxychloroquine in fighting COVID-19 pandemic: synthesis and characterization, Inorg. Chem. Commun. 126 (2021) 108472.
[2] P.W. Choppin, R.W. Compans, Reproduction of paramyxoviruses, in: Comprehensive Virology, Springer, Boston, MA, 1975, pp. 95–178.
[3] S.T. Nichol, J. Arikawa, Y. Kawaoka, Emerging viral diseases, Proc. Natl. Acad. Sci. USA. 97 (23) (2000) 12411–12412.
[4] W. Parry, E. Peterson, Devastating infectious Diseases, Live sci, 2020.
[5] A.Z. Mirza, H. Shamshad, F.A. Osra, T.M. Habeebullah, M. Morad, An overview of viruses discovered over the last decades and drug development for the current pandemic, Eur. J. Pharmacol. 890 (2021) 173746.
[6] M. Cascella, M. Rajnik, A. Cuomo, S.C. Dulebohn, R. Di Napoli, Features, Evaluation, and Treatment Coronavirus (COVID-19). StatPearls publishing, 2020.
[7] J. Blaising, S.J. Polyak, E.-I. Pécheur, Arbidol as a broad-spectrum antiviral: an update, Antivir. Res. 107 (2014) 84–94.
[8] X.X. Du, X.P. Chen, Favipiravir: pharmacokinetics and concerns about clinical trials for 2019-nCoV infection, Clin. Pharmacol.. Ther. 108 (2020) 242–248.
[9] P. Tarighi, S. Eftekhari, M. Chizari, M. Sabernavaei, D. Jafari, P. Mirzabeigi, A review of potential suggested drugs for coronavirus disease (COVID-19) treatment, Eur. J. Pharmacol. 895 (2021) 173890.
[10] W.H. Prusoff, Synthesis and biological activities of iododeoxyuridine, an analog of thymidine, Biochimica. Biophysica. Acta. 32 (1) (1959) 295–296.
[11] K.R. Wilhelmus, Antiviral treatment and other therapeutic interventions for herpes simplex virus epithelial keratitis, Cochrane Database Syst. Rev. 1 (2015) CD002898.

[12] A.S. Sokolova, O.I. Yarovaya, N.I. Bormotov, L.N. Shishkina, N.F. Salakhutdinova, Synthesis and antiviral activity of camphor-based 1,3-thiazolidin-4-one and thiazole derivatives as Orthopoxvirus -reproduction inhibitors, Med. Chem. Comm. 9 (10) (2018) 1746–1753.
[13] (a) S. Cascioferro, B. Parrino, D. Carbone, D. Schillaci, E. Giovannetti, G. Cirrincione, P. Diana, Thiazoles, their benzofused systems, and thiazolidinone derivatives: versatile and promising tools to combat antibiotic resistance, J. Med. Chem. 63 (15) (2020) 7923–7956; (b) B.R Beno, K. Yeung, M.D Bartberger, L.D Pennington, N.A Meanwell, A Survey of the role of noncovalent sulfur interactions in drug design, J. Med. Chem. 58 (2015) 4383–4438.
[14] S.R. Shih, T.Y. Chu, G.R. Reddy, S.N. Tseng, H.L. Chen, W.F. Tang, M.S. Wu, J.Y. Yeh, Y.S. Chao, J.T. Hsu, H.P. Hsieh, J.T. Horng, Pyrazole compound BPR1P0034 with potent and selective anti-influenza virus activity, J. Biomed. Sci. 17 (2010) 1–9.
[15] N.V. Makarova, E.I. Boreko, I.K. Moiseev, N.I. Pavlova, S.N. Nikolaeva, M.N. Zemtsova, G.V. Vladyko, Antiviral activity of adamantane-containing heterocycles, Pharm. Chem. J. 36 (2002) 3–6.
[16] R.G. Corbau, C.E. Mowbray, M. Perros, P.A. Stupple, A. Wood, Pyrazole derivatives useful as reverse transcriptase inhibitors, for the treatment of HIV infection, and their use, formulations, and preparation, PCT Int. Appl. (2002) WO 2002004424 A1 20020117.
[17] S. Colarusso, B. Attenni, S. Avolio, S. Malancona, S. Harper, S. Altamura, U. Koch, F. Narjes, Inhibitors of the hepatitis C virus RNA-dependent RNA polymerase, Arkivoc. vii (2006) 479–495.
[18] S. Yan, T. Appleby, G. Larson, J.Z. Wu, R. Hamatake, Z. Hong, N. Yao, Structure based design of a novel thiazolone scaffold as HCV NS5B polymerase allosteric inhibitors, Bioorg. Med. Chem. Lett. 16 (2006) 5888–5891.
[19] K.M. Dawood, T.M.A. Eldebss, H.S.A. El-Zahabi, M.H. Yousef, Synthesis and antiviral activity of some new bis-1,3-thiazole Derivatives, Eur. J. Med. Chem. 102 (2015) 266–276.
[20] M. Kalanithi, D. Kodimunthiri, M. Rajarajan, P. Tharmaraj, Synthesis, characterization and biological activity of some new VO(IV), Co(II), Ni(II), Cu(II) and Zn(II) complexes of chromone based NNO Schiff base derived from 2-aminothiazole, Spectrochimica. Acta. Part A 82 (1) (2011) 290–298.
[21] A. Lewis, M. McDonald, S. Scharbach, S. Hamaway, M. Plooster, K. Peters, K.M Fox, L. Cassimeris, J.M Tanski, L.A Tyler, The chemical biology of Cu(II) complexes with imidazole or thiazole containing ligands: Synthesis, crystal structures and comparative biological activity, J. Inorg. Biochem. 157 (2016) 52–61.
[22] A.I. Vogel, Quantitative Inorganic Analysis, Longmans, London, 1989.
[23] M. Frisch, G. Trucks, H. Schlegel, G. Scuseria, M. Robb, J. Cheeseman, G. Scalmani, V. Barone, B. Mennucci, G. Petersson, Gaussian 09, Revision A1, Gaussian, Wallingford, CT, USA, 2009.
[24] A.D. Becke, Density-functional thermochemistry. III. The role of exact exchange, J. Chem. Phys. 98 (7) (1993) 5648–5652.
[25] C. Lee, W. Yang, R.G. Parr, Development of the Colle-Salvetti correlation-energy formula into a functional of the electron density, Phys. Rev. B 37 (2) (1988) 785–789.
[26] J.P. Perdew, Y. Wang, Pair-distribution function and its coupling-constant average for the spin-polarized electron gas, Phys. Rev. B 46 (20) (1992) 12947–12954.
[27] R. Dennington, T. Keith, J. Millam, GaussView, Version 5, Semichem Inc., Shawnee Mission, KS, 2009.
[28] C.D. Willey, J.A. Bonner. Interaction of chemotherapy and radiation gunderson LL, tepper JEBT-CRO (Third E, editors. clin. radiat. oncol. 3rd editio, philadelphia: W.B. saunders) (2012) 65–82.
[29] J. Sunseri, D.R. Koes, Pharmit: interactive exploration of chemical space, Nucl. Acids Res 44 (W1) (2016) W442–W448.
[30] T.M. Musyoka, A.M. Kanzi, K.A. Lobb, Ö.T. Bishop, Structure based docking and molecular dynamic studies of plasmodial cysteine proteases against a South African natural compound and its analogs, Sci. Rep. 6 (2016) 1–12.
[31] S.Y. Al-nami, E. Aljuhani, I. Althagafi, H.M. Abumelha, T.M. Bawazeer, A.M. Al–Solimy, Z.A. Al-Ahmed, F. Al-Zahrani, N. El-Metwaly, Synthesis and Characterization for new nanometer Cu (II) complexes, conformational study and molecular docking approach compatible with promising in vitro screening, Arab. J. Sci. Eng. 46 (1) (2021) 365–382.
[32] M.S. Refat, A. Bayazeed, H. Katouah, R. Shah, M. Morad, M. Abualnaja, S. Alsaigh, F. Saad, N. El-Metwaly, In-silico studies for kinetin hormone and its alkaline earth metal ion complexes as anti-aging cosmetics; synthesis, characterization and ability for controlling collagen-inhibitors, J. Mol. Struct. 1232 (2021) 130041.
[33] R. Shah, H. Katouah, A.A. Sedayo, M. Abualnaja, M.M. Aljohani, F. Saad, R. Zaky, N.M. El-Metwaly, Practical and computational studies on novel Schiff base complexes derived from green synthesis approach: conductometry as well as in-vitro screening supported by In-silico study, J. Mol. Liq. 319 (2020) 114116.
[34] W.J. Geary, The use of conductivity measurements in organic solvents for the characterization of coordination compounds, Coord. Chem. Rev. 7 (1971) 81–122.
[35] A.M. Abu-Dief, N.M. El-Metwaly, S.O. Alzahrani, F. Alkhatib, M.M. Abualnaja, T. El-Dabea, M. Abd El Aleem Ali Ali, Synthesis and characterization of Fe (III), Pd (II) and Cu (II)-thiazole complexes; DFT, pharmacophore modeling, in-vitro assay and DNA binding studies, J. Mol. Liq. 326 (2021) 115277.
[36] K. Nakamoto, in: Infrared Spectra of Inorganic, Co-ordination Compounds, 25, Wiley Interscience, New York, 1970, pp. 232–239.
[37] A.B.P. Lever, Inorganic Electronic Spectroscopy, 2nd ed., Elsevier, New York, 1984.
[38] G.A.A. Al-Hazmi, K.S. Abou-Melha, N.M. El-Metwaly, I. Althagafi, F. Shaaban, M.G. Elghalban, M.M. El-Gamil, Spectroscopic and theoretical studies on Cr (III), Mn (II) and Cu (II) complexes of hydrazone derived from picolinic hydrazide and O-vanillin and evaluation of biological potency, Appl. Organomet. Chem. 34 (2019) e5408.
[39] F. Alkhatib, A. Hameed, A. Sayqal, A.A. Bayazeed, S. Alzahrani, Z.A. Al-Ahmed, R. Zaky, N.M. El-Metwaly, Green-synthesis and characterization for new Schiff-base complexes; spectroscopy, conductometry, Hirshfeld properties and biological assay enhanced by in-silico study, Arab. J. Chem. 13 (8) (2020) 6327–6340.
[40] M.S. Refat, N.M. El-Metwaly, Spectroscopic and fluorescence studies on Mn (II), Co (II), Ni (II) and Cu (II) complexes with NO donor fluorescence dyes, Spectrochim. Acta A 81 (2011) 215–256.
[41] B.J. Hathaway, A new look at the stereochemistry and electronic properties of complexes of the copper(II) ion, Struct. Bonding (Berlin) 57 (1984) 55–118.
[42] J.A. Welleman, F.B. Hulsbergen, Influence of alkyl chain length in N-alkyl imidazoles upon the complex formation with transition-metal salts, J. Inorg. Nucl. Chem. 40 (1978) 143–147.
[43] H.A. Katouah, J.H. Al-Fahemi, M.G. Elghalban, F.A. Saad, I.A. Althagafi, N.M. El-Metwaly, A.M. Khedr, Synthesis of new Cu (II)-benzohydrazide nanometer complexes, spectral, modeling, CT-DNA binding with potential anti-inflammatory and anti-allergic theoretical features, Mater. Sci. Eng. C. 96 (2019) 740–756.
[44] M.S. Refat, N.M. El-Metwaly, Spectral, thermal and biological studies of Mn (II) and Cu (II) complexes with two thiosemicarbazide derivatives, Spectrochim. Acta A 92 (2012) 336–346.
[45] B.D. Cullity, Elements of X –ray diffraction, Second ed., Addison –Wesley Inc., 1993.
[46] S. Velumani, X. Mathew, P.J Sebastian, Sa.K. Narayandass, D. Mangalaraj, Sol. Energ. Mat. Sol. Cell. 76 (3) (2003) 347–358.
[47] S. Alzahrani, M. Morad, A. Bayazeed, M. Aljohani, F. Alkhatib, R. Shah, H. Katouah, H.M. Abumelha, I. Althagafi, R. Zaky, N.M. El-Metwaly, J. Mol. Struct. 1218 (2020) 128473.
[48] H. Katouah, A.M. Hameed, A. Alharbi, F. Alkhatib, R. Shah, S. Alzahrani, R. Zaky, N.M. El-Metwaly., ChemistrySelect 5 (33) (2020) 10256–10268.
[49] P. Mu, R. Karuppasamy, Discovery of human autophagy initiation kinase ULK1 inhibitors by multi-directional in silico screening strategies, J. Recept. Signal Transduct. 39 (2) (2019) 122–133.
[50] N. Kandakatla, G. Ramakrishnan, Ligand based pharmacophore modeling and virtual screening studies to design novel HDAC2 inhibitors, Adv. Bioinform. 2014 (2014) 812148.
[51] A.S. Obrecht, N. Urban, M. Schaefer, A. Röse, A. Kless, J.E. Meents, A. Lampert, A. Abdelrahman, C.E. Müller, G. Schmalzing, R. Hausmann, Identification of aurintricarboxylic acid as a potent allosteric antagonist of P2X1 and P2X3 receptors, Neuropharmacology 158 (2019) 107749.
[52] M.V. Angelusiu, S.F. Barbuceanu, C. Draghici, G.L. Almajan, New Cu (II), Co (II), Ni (II) complexes with aroyl-hydrazone based ligand. Synthesis, spectroscopic characterization and in vitro antibacterial evaluation, Eur. J. Med. Chem. 45 (5) (2010) 2055–2062.
[53] K. Kuca, K. Musilek, D. Jun, J.Z. Karasova, E. Nepovimova, O. Soukup, M. Hrabinova, J. Mikler, T.C.C. Franca, E.F.F. Da Cunha, A.A. De Castro, M. Valis, T.C. Ramalho, A newly developed oxime K203 is the most effective reactivator of tabun-inhibited acetylcholinesterase, BMC Pharmacol. Toxicol. 19 (1) (2018) 1–10.